

Physical, electrical, transport and magnetic properties of Nd(Ba,Nd)_{2.1}Cu₃O_{7- δ} system

E. Altin · D. M. Gokhfeld · F. Kurt ·
Z. D. Yakinci

Received: 16 July 2013 / Accepted: 3 October 2013 / Published online: 13 October 2013
© Springer Science+Business Media New York 2013

Abstract In this study, the superconducting Nd(Ba,Nd)_{2.1}Cu₃O_{7- δ} system has been prepared using conventional solid-state reaction technique. Transport properties including structural/microstructural evolution, electrical, magnetic and critical current density properties were investigated. After high temperature heat treatments at over 1,000 °C, large and strongly connected grains were obtained but weakly connected and small in size granular formation were obtained for the low temperature heat treated samples at around 900 °C. The best T_c and T_0 values were obtained as 93 and 89 K respectively for the sample prepared at 1,020 °C for 24 h, which is very close to peritectic temperature of YBCO material. Magnetization of the sample heat treated at 1,020 °C was investigated in detail. The magnetization hysteresis loops are expounded to be the product of Nd-123 grains and unscreened Nd³⁺ ions within intergranular boundaries and vortex cores. The peak effect on the magnetization curves was described by the extended critical state model. Temperature dependencies of the irreversibility field, the peak field and the full penetration field correlate and there is scaling behavior of the pinning force as well. Thermoelectric power data was analyzed by “Modified two band model with linear T-term

for superconductors”. Temperature dependence of thermal conductivity of the samples showed small peak with broad maximum just below the T_c value. Thermal conductivity of samples prepared was calculated by using “The Modified Callaway Model and Wiedermann–Franz law” and results obtained discussed.

1 Introduction

After discovery of superconductivity in YBa₂Cu₃O_{7- δ} (Y-123) compound at 90 K, above liquid nitrogen temperature (77 K), many studies were done on this compound to improve T_c and J_c values [1–5]. Particularly, rare earth elements (Re = Nd, Eu, Sm, etc.) were frequently substituted/doped into the Y site to improve the microstructure and transport properties of the system [6–10]. According to results obtained, the T_c value of the Re-123 system remained almost unchanged but the J_c value changed from 10⁴ to 10⁶ A/cm² depending on Re element. This phenomenon has been attributed to the crystalline defects such as dislocations, impurities, stacking faults, grain boundaries, which improve the magnetic flux pinning mechanism in the superconducting state and so the J_c value of the samples. This peculiarity makes RE-123 a suitable candidate particularly for technological applications of thin/thick films or large area coatings including bulk magnet fabrication.

Takekawa et al. [11], the first to study the Nd(Nd_zBa_{2-z})Cu₃O_y system, found the formation of the solid solutions phase when substitution is $0 \leq z \leq 0.8$. According to their results, at room temperature, the Nd_{1+z}Ba_{2-z}Cu₃O_y phase has orthorhombic symmetry for z ranging from 0 to 0.14 and tetragonal symmetry for $z > 0.2$. After the observation of 94 K transition in NdBa₂Cu₃O_y material with Nd

E. Altin (✉) · F. Kurt
Bilimsel ve Teknolojik Araştırma Merkezi, İnönü Üniversitesi,
44280 Malatya, Turkey
e-mail: emine.altin@inonu.edu.tr

D. M. Gokhfeld
L.V. Kirensky Institute of Physics SB RAS, Akademgorodok
50/38, 660036 Krasnoyarsk, Russia

Z. D. Yakinci
Sağlık Hizmetleri Meslek Yüksek Okulu, İnönü Üniversitesi,
44280 Malatya, Turkey

substitution for Ba, the studies have been accelerated to improve the transport properties of this material. Recently results obtained showed that both J_c and T_c of this material are slightly higher than the YBCO superconductors especially under high magnetic field experiments [12–17]. Particularly easy relocation ability in crystal structure and also reasonably good diffusion properties of both Nd and Ba atoms, that produces homogeneous phase distribution and grain growth, resulted in well oriented and strongly connected grains formation with high J_c and T_c properties at the same time. Formation of solid solution phase, which is necessary particularly for the high J_c achievement, is important for Re-123 systems. In the studies in literature, it was noticed that formation of solid solution phase at 1,000–1,060 °C significantly improves dislocations/diffusion of atoms to form good grain connectivity without any impurity phase formation within the grains border [18–20].

For characterization of superconducting materials and for their technological applications the elastic constants, specific heat, electrical conductivity, thermoelectric power etc. are the important physical properties. Many research groups studied the thermoelectric power and thermal conductivity properties of Y-123, Bi-2212, and Tl-1223 systems with many doping/substitutions. But there exist no results in the literature about the transport properties of $\text{Nd}(\text{Ba,Nd})_{2.1}\text{Cu}_3\text{O}_{7-\delta}$ material which may play an important role for their advance applications particularly in electronic devices fabrication [21].

In this study, we successfully fabricated $\text{Nd}(\text{Ba,Nd})_{2.1}\text{Cu}_3\text{O}_{7-\delta}$ compounds using solid state reaction method with different heat treatment cycles. Physical, electrical, magnetic and transport properties including thermal conductivity and thermoelectric power were investigated and the results obtained were discussed.

2 Experimental details

In this work, bulk samples were prepared using conventional solid-state reaction technique. High purity (99.9 %) powders of Nd_2O_3 , BaCO_3 and CuO (Alfa-Aesar) were weighed in the appropriate amounts to give nominal composition of $\text{Nd}(\text{Ba,Nd})_{2.1}\text{Cu}_3\text{O}_{7-\delta}$. The powders were mixed in an agate mortar and then heat treated at 900 °C for 24 h with intermediate grinding and mixing. The powders were pressed into pellets under pressure of 65 MPa. The pellets were heat treated between 880 and 1,120 °C for 24 h under oxygen atmosphere. Heating and cooling rates were chosen as 10 °C min^{-1} .

The structural characterization of the samples prepared was investigated by X-ray diffraction (XRD). Automated Rigaku RadB Dmax-II X-ray diffractometer having CuK_α radiation was used. Scan speed was selected as 2° min^{-1}

in the range of $2\theta = 30\text{--}80^\circ$. The lattice parameters of the samples were calculated Rietveld-Refinement method using Jade 5.0 software.

The microstructural and compositional characterization of the samples was performed using Leo EVO-40 VPX scanning electron microscope (SEM) and BRUKER X-flash Energy Dispersive X-ray Spectroscopy (EDX).

Temperature dependence of resistivity (ρ - T) of the samples was measured by closed cycle Leybold LT-10 cryostat system with SRS AC bridge system using 17.7 Hz frequency. The T_c value was determined as the peak temperature in $d\rho(T)/dT$ plot.

Magnetic, thermoelectric power and thermal conductivity measurements were performed by using Quantum Design PPMS-9T system. The thermoelectric power data were analyzed with “Modified two band model with linear T term for superconductors” and the results obtained were discussed. For thermal conductivity calculations, we used “Modified Callaway model”, that uses lattice component [22] and “Wiedemann–Franz” law which is related with the electronic component of thermal conductivity [23], thus both lattice and electronic components were summed. The Bean formula, for polycrystalline superconductors, was applied to calculate the averaged critical current density of samples. The dependence of the pinning force to the applied magnetic field was determined from $F_p(H) = I_c(H) \times H$ formula.

3 Results and discussion

3.1 XRD analysis

X-ray diffraction patterns of the samples heat treated at different temperatures are shown in Fig. 1. All peaks in the XRD patterns were assigned to $\text{Nd}(\text{Ba,Nd})_{2.1}\text{Cu}_3\text{O}_{7-\delta}$ material without any impurity phases. This obviously shows that the diffusion mechanism, which is essential for formation of single phase material, is well constituted during heat treatment cycle. However, slightly different XRD patterns were obtained between the samples heat treated at 880 and 1,100 °C. Particularly peak intensity of high temperature heat treated sample (1,100 °C) decreased sharply but position of the peaks remained unchanged. Samples heat treated up to 1,000 °C showed almost similar characteristics but shape of the peaks started to change when heat treatment temperature is increased further. Particularly peaks obtained after $2\theta = 45^\circ$ splitted into two parts showing that the formation of well defined orthorhombic symmetry for Nd-123 material as obtained previously in the literature [24]. After Rietveld refinement of the XRD data, it was determined that all samples have an orthorhombic symmetry but calculated unit cell parameters

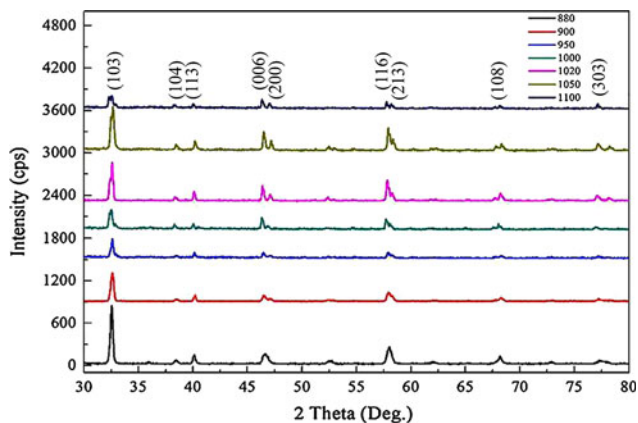


Fig. 1 XRD patterns of the Nd-based system prepared under different heat treatment conditions

Table 1 Structural and microstructural results of the samples prepared under different heat treatment temperatures

Heat treatment Temperature (°C)	Symmetry	<i>a</i> (Å)	<i>b</i> (Å)	<i>c</i> (Å)
880	Orthorhombic	3.876	3.890	11.699
900	Orthorhombic	3.858	3.901	11.724
950	Orthorhombic	3.861	3.905	11.725
1,000	Orthorhombic	3.874	3.885	11.758
1,020	Orthorhombic	3.864	3.912	11.717
1,050	Orthorhombic	3.855	3.903	11.721
1,100	Orthorhombic	3.863	3.905	11.750

were showed a slight variation depending on the heat treatment temperature, Table 1.

3.2 Micro-structural analysis

The surface morphologies of the samples obtained are shown in Fig. 2a–g. As seen in the figure, a poorly connected grains with high degree of porosity were obtained for the samples heat treated at 880–900 °C suggesting an insufficient heating treatment cycles. The grains sizes ranging between 1 and 5 μm were seen clearly. When the heat treatment temperature was increased to 950 °C and above such as 1,000–1,050 °C, Fig. 2c–h, much more compacted and strongly connected large grains with the size of 5–20 μm were formed largely. The porosity on the surface of the samples was disappeared completely. At high temperatures such as 1,050–1,150 °C a partly melted surface morphology and spiral/helix like layer by layer grain growth, were obtained, Fig. 2g, h. This kind of crystal growth generally obtained during the single crystal oxide material fabrication. For the superconductor material fabrication such a large and strongly connected grains formation is important particularly for transport properties

of the samples due to the minimum scattering of the charge carriers from the large grains and so the low overall resistivity of the samples can be achieved, Fig. 3.

3.3 Electrical properties

Temperature dependence of the resistivity of the samples prepared at different heat treatments are shown in Fig. 3 and the data obtained are summarized in Table 2. The sample prepared at 880 °C for 24 h (low temperature treated samples) exhibited highest normal state resistance and the tail after T_c was enlarged significantly. It is believed that the possible cause of high resistivity can be due to the porosities and weakly connected small grains formation all over the sample which is hardly related with the insufficient thermal treatment. T_c and T_0 of the sample prepared at 880 °C for 24 h were found to be at 88 and 62 K, respectively. When the heat treatment temperature was increased the normal state resistance decreased sharply, samples show a metallic behavior at high temperature region followed by a superconducting transition as the temperature was lowered and so the T_c and T_0 values of the samples were increased. The best T_c and T_0 values were obtained to be 93 and 89 K respectively for the sample prepared at 1,020 °C for 24 h.

3.4 Thermoelectric power analysis (TEP)

Temperature dependence of thermoelectric power (S - T) for (Nd(Ba,Nd)_{2.1}Cu₃O_{7-δ}) samples fabricated at 900 and 1,050 °C are shown in Fig. 4 as an example. The S values were found to be positive between room temperature to 5 K, suggesting that the holes are dominant charge carriers in the samples. However we obtained two different properties for low (900 °C) and high (1,050 °C) temperature heat treated samples. The TEP of the sample heat treated at 900 °C showed a decrease by decreasing the temperature down to T_c and then diminished when it reach to 77 K. In the case of the sample heat treated at 1,050 °C, firstly the TEP increased up to T_c and then dropped to the zero at 87 K.

This kind of behavior has been obtained for YBCO material previously by many research groups and can be explained with the planar or chain nature of materials prepared. According to Neeleshwar et al. the crystallographic plane contribution to TEP in the YBCO system gives a negative slope, whereas the contribution of the chains has a positive slope [25]. It can be easily said that the plane contribution is dominant for the samples fabricated at 900 °C, while the chain contribution is dominant for the sample heat treated at 1,050 °C which is the classical nature of perfectly crystalized YBCO based materials.

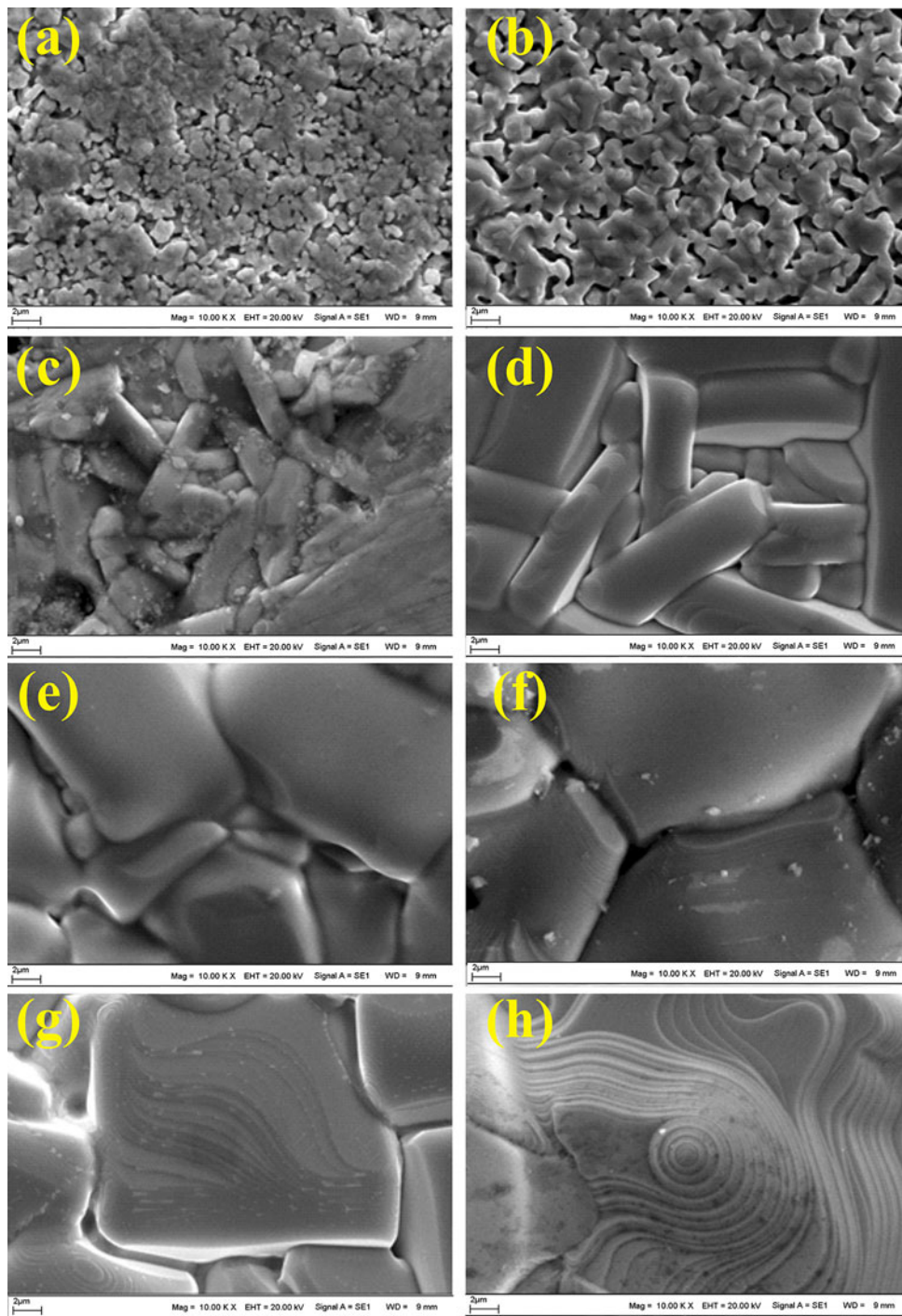


Fig. 2 SEM images of the samples prepared at (a) 880 °C, (b) 900 °C, (c) 950 °C, (d) 1,000 °C, (e) 1,020 °C, (f) 1,050 °C and (g) 1,100 °C for 24 h

Theoretically TEP property of superconductor materials can be explained with different models such as, fluctuation effects, electro-phonon enhancement effect, trapping effect etc. On the other hand, temperature dependence of TEP of the HT_c superconductor materials shows a similarity with

mixed valence heavy fermion systems [26]. For example Gottwick et al. [27] analyzed the TEP data of CeNi samples assuming a Lorentzian resonance near the Fermi level. In order to analyze the data, they used the formulas given below:

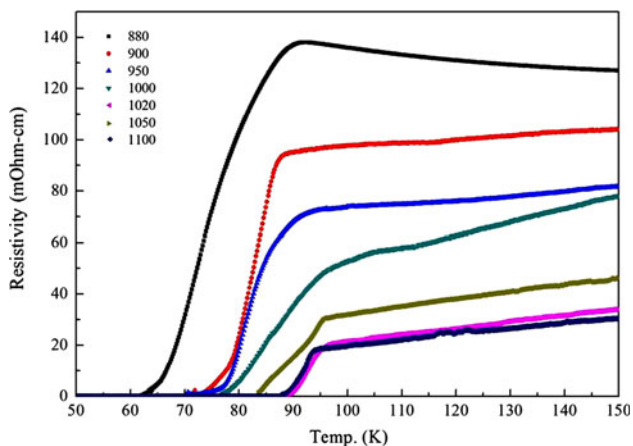


Fig. 3 Temperature dependence of resistance the samples prepared at different heat treatment temperatures

Table 2 T_c and T_o values of the samples

Heat treatment temperature (°C)	Electrical measurements	
	T_c (K)	T_o (K)
880	88	62
900	87	72
950	92	75
1,000	94	79
1,020	97	89
1,050	94	87
1,100	94	83

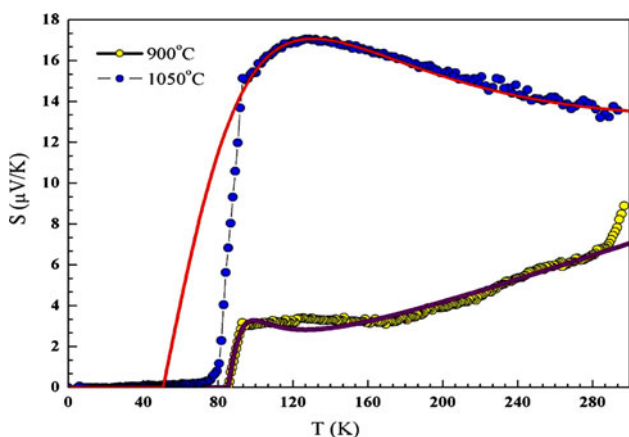


Fig. 4 Temperature dependence of thermoelectric power for NdBCO samples fabricated with heat treatment temperature for 900 and 1,050 °C and the fitting results according to modified two band model with linear T term for superconductors

$$S = \frac{AT}{B^2 + T^2} \tag{1}$$

$$A = \frac{2(E_o - E_F)}{e} \tag{2}$$

$$B = \sqrt{3 \frac{(E_o - E_F)^2 + \gamma^2}{\pi^2 k_B^2}} \tag{3}$$

where AT shows the conduction of metallic holes and B/T the conduction of the semiconductor type electrons. E_o and γ are center and width of the resonance, respectively. The theory is based on a localized band in density of states near the Fermi level, which is superimposed on a broad band. This resonance peak gives the characteristic temperature dependence of TEP. In addition to this, Forro et al. [28] indicated that the temperature dependence of TEP in the HT_c systems has a similar structure with mixed valent heavy fermion systems. In order to explain the temperature dependence of TEP in the HT_c superconductors they added a linear term to Eq. 1 for fitting:

$$S = \frac{AT}{B^2 + T^2} + \alpha T \tag{4}$$

where αT represents normal band contribution. In this model, electrons and holes have different mobilities. Equation 4 was used for fitting the TEP data by many research groups and results obtained showed good fitting with experimental results especially above T_c [29–31]. But, this model can not explain behavior of TEP below T_c . According to the model, TEP goes zero at 0 K but TEP experimentally goes to zero just below T_c for the HT_c superconducting materials. Thus, the T_c value of superconductors plays a crucial role on TEP data.

In the present work, the TEP data was analyzed with “Two Band Model with Linear T-Term” by modifying the temperature term. As mentioned above TEP is expected to become zero at 0 K, but for the superconducting materials TEP drops to zero just below T_c . So, in order to compensate this contradiction, we replaced the temperature, T , with $(T - T^*)$ in Eq. 4, as given below:

$$S = \frac{A(T - T^*)}{B^2 + (T - T^*)^2} + \alpha(T - T^*) \tag{5}$$

Where T^* is the temperature of zero TEP for superconductors. It was fitted the experimental TEP data to Eq. 5 and the fitting parameters are given in Table 3. According to our results a good agreement with experimental TEP data and fitting was obtained for all the samples as given in Fig. 4. Although only a little difference between the T^* and T_o , we predict that both are equal to each other.

3.5 Thermal conductivity analysis

Figure 5 shows the experimental data of temperature dependence of thermal conductivity, $\kappa(T)$, and fitting results according to the sum of lattice component of

Table 3 The fitting parameters of TEP and Thermal conductivity

Heat treatment temp. (°C)	A	B	α	T*		
Thermoelectric power						
900	68.57	11.886	0.0314	85.17		
1,050	2,211.43	71.543	0.0214	50.6		
Heat treatment temp. (°C)	α	β	γ	δ	A	B
Thermal conductivity						
900	11.02	20	8.16	132.65	45.92	1.1E – 5
1,050	35.51	14.90	8.98	131.63	78.57	0.00357

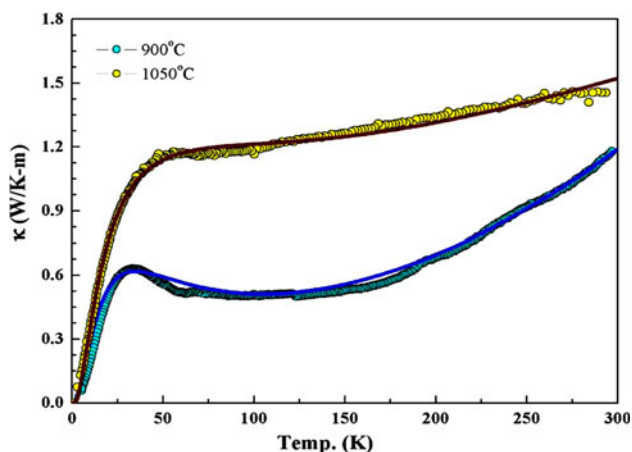


Fig. 5 Temperature dependence of thermal conductivity for NdBCO samples fabricated with heat treatment temperature for 900 and 1,050 °C and the fitting results according to the sum of lattice component of thermal conductivity with the modified Callaway model and electronic component of thermal conductivity by Wiedermann–Franz law

thermal conductivity with “Modified Callaway model” and electronic component of thermal conductivity from “Wiedermann–Franz law”. As seen in Fig. 5, for the sample heat treated at 1,050 °C, the $\kappa(T)$ is decreased smoothly down to T_c with linear T dependence. But for the sample heat treated at 900 °C a different behavior of $\kappa(T)$ – T dependence was obtained. Before the peak with broad maximum, obtained just before the T_c , a sharp decrease on the $\kappa(T)$ was obtained with T^2 dependence. In general, this kind of behavior has not been observed in the HT_c systems [32–36]. The origin of broad maximum in $\kappa(T)$ is not clear but mainly two mechanisms have been proposed to explain it. The first mechanism explains the sharp rise in $\kappa(T)$ with the increase of phonon mean free path as electrons condense into Cooper pair [37]. An alternative mechanism ascribes the broad maximum to the electron contribution [38]. However, in the recent theoretical and experimental studies suggested that the broad

maximum of $\kappa(T)$ just below T_c , can be related with enhancement of the quasiparticle contribution to the heat conductivity. Because quasiparticle life-time and quasiparticle mean free path abruptly increase in the superconducting state. This causes an increase in the electronic heat transport [39–41].

It is well known that $\kappa(T)$ of samples consists sum of lattice contribution and electronic contribution [42]:

$$\kappa = \kappa_e + \kappa_L \quad (6)$$

The electronic contribution in normal-state, above T_c , can be calculated from the Wiedermann–Franz law:

$$\kappa_{en} \leq \frac{L_0 T}{\rho} \sim BT \quad (7)$$

where L_0 is the Lorentz number ($2.45 \times 10^{-8} \Omega\text{WK}^{-2}$) and $\rho(T)$ the resistivity. In this calculation electronic component of thermal conductivity shows linear temperature dependence. Together with this lattice component, κ_L , of thermal conductivity can be written in the following form by introducing the reduced frequency and the reduced temperature [22]:

$$\kappa_L = At^3 \int_0^\infty \frac{x^4 e^x}{(e^x - 1)^2 F(t; x)} dx \quad (8)$$

where $F(t, x)$ represents the total relaxation rate [42] and given by:

$$F(t; x) = (1 + \alpha x^4 t^4 + \beta x^2 t^2 + \gamma t x g(x; y) + \delta x^3 t^4 + (\varepsilon_1 + \varepsilon_2 e^{-\theta a T}) x^2 t^5) \quad (9)$$

Here A , α , β , γ , δ , ε_1 and ε_2 refer to the scattering strength due to the boundary scattering, point defect scattering, sheet-like fault, electron–phonon scattering, interference scattering (between point defect and 3-phonon process) 3-phonon normal and U-scattering, respectively. According to ref [42] A was taken 0.01 in our calculations. $g(x, y)$ is Bardeen-Rickayzen-Tewordt (BRT) function as given below [43–47]:

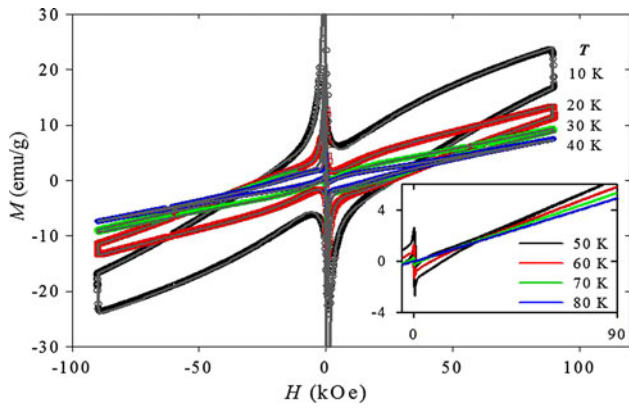


Fig. 6 Hysteretic magnetization curves of Nd-123 heat treated at 1,020 °C

$$g(x; y) = \frac{2F_1(-y) + 2y \ln(1 + e^{-y}) + \frac{y^2}{1+e^y}}{2F_1(0)} \quad (10)$$

where

$$y = \frac{\Delta(T)}{k_B T} \quad (11)$$

and

$$F_n(-y) = \int_0^\infty \frac{Z^n}{1 + e^{Z+y}} dZ \quad (12)$$

which is a Fermi–Dirac functions of integral order.

The best fitting parameters were calculated by using Eq. 8 and experimental data obtained in this work, which are given in Table 3. A good agreement between the experimental results and calculations was observed, Fig. 5. The boundary scattering parameter, A , is the highest value for the sample heat treated at 1,050 °C, but it decreases when the heat treatments temperature decreased. This is expected because samples heat treated at around 900 °C showed a small and merged granular formation and this produces more contact points between the grains comparing to sample heat treated at 1,050 °C which has rather large granular formation with sharp grain boundaries. Other parameters such as B , γ and α also showed similar trend and supports the effect of crystallization on the fitting parameters. The sheet-like fault parameter, β , of the high temperature heat treated sample showed approximately 100 times higher value than the 900 °C heat treated sample indicating that the better microstructural formation for the high temperature heat treated sample. The point defect scattering parameter value, α , was increased with heat treatment. The sheet-like fault parameter, β , gives a decrease with increasing heat treatment temperature. The electron–phonon scattering parameter, γ , has close values for both samples. The strength parameter of electronic

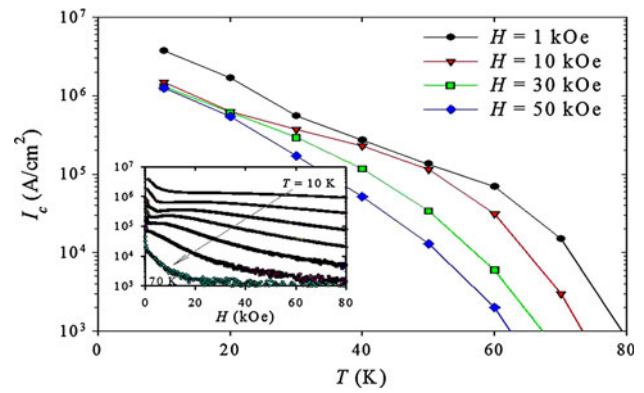


Fig. 7 Critical current density of Nd-123 heat treated at 1,020 °C. Temperature dependence of J_c . Lines are a guide for eyes. Insert demonstrates $J_c(H)$ dependence at different temperatures (10–70 K)

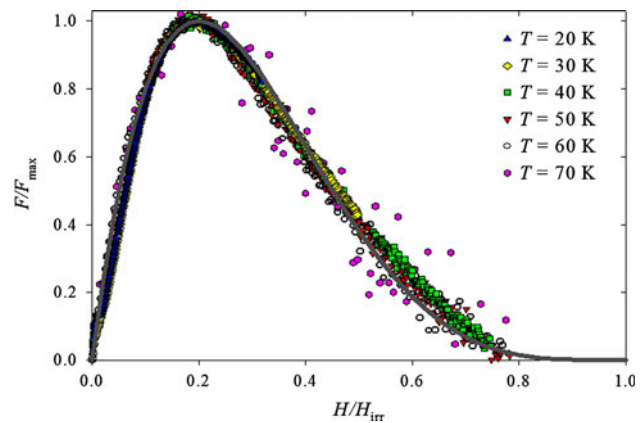


Fig. 8 Scaling of pinning force of Nd-123 heat treated at 1,020 °C

component of thermal conductivity, B , is a parameter, depending on the carrier concentration of samples. The B value for the sample prepared at 900 °C is higher than the sample prepared at 1,050 °C.

3.6 Magnetic properties

Figure 6 shows magnetic hysteresis loops of Nd(Ba,Nd)_{2.1}Cu₃O_{7-δ} samples at 10–80 K. The hysteresis loops are tilted in the anticlockwise direction. The magnetization of the sample changes its sign from the negative to positive at H equal to 2.59 T at $T = 10$ K. This point then decreases rapidly with increasing the temperature and decreased to 0.07 T at $T = 80$ K.

The Bean formula for polycrystalline superconductors was applied to find the sample averaged critical current density: $J_c = 30\Delta M/d$ in A/cm², here ΔM is the hysteresis loop width in emu/cm³ and d is the average grain size in cm [48]. For Nd(Ba,Nd)_{2.1}Cu₃O_{7-δ} sample heat treated at 1,020 °C the averaged grain size determined from SEM photos is 8 μm. The behavior of J_c at different T and H are

plotted on Fig. 7. The $J_c(H)$ dependencies demonstrate the fishtail effect with a spreading peak (insert in Fig. 7). Due to this peak, the sample has a high critical current density right up to highest fields at a wide temperature range.

The dependence of the pinning force density on the applied magnetic field was determined from $F_p(H) = J_c(H) \times H$. The peak position H_{peak} on $F_p(H)$ curves is approximately 2 times larger than the second maximum position on the $J_c(H)$ curves at any temperature (T). On Fig. 8 the normalized pinning force $f = F_p/F_{p\text{max}}$ is plotted as a function of the reduced field $h = H/H_{\text{irr}}$, where $F_{p\text{max}}$ is the maximal pinning force density, H_{irr} is the irreversibility field. To define accurately H_{irr} , the $J_c(H)$ curves were decreased on the noise level. The value of H_{irr} at $T = 10$ K is much more than the maximal applied field and cannot be located. Also the data for $T = 80$ K are omitted on Fig. 8 due to a high noise level. The resulted $f(h)$ curves are coincide: all points lay on the one curve and the peak of pinning is at $h = 0.2$ at all temperatures. The scaling law $F_p(H, T) = F_{p0}(T)h^p(1-h)^q/(h_0^p(1-h_0)^q)$ [49] was applied to the $f(h)$ curves, here h_0 is the position of the maximum, $h_0 = p/(p+q)$. The scaling is performed for $p = 1$ and $q = 4$ instead the Kramer parameters ($p = 0.5$ and $q = 2$) [50]. Unfitness of the Kramer parameters is rather typical for high-temperature superconductors [51].

The measured $M-H$ curves are the superposition of a hysteresis loop $M_S(H)$ of the superconducting crystallites and a paramagnetic magnetization curve $M_P(H)$: $M(H) = M_S(H) + M_P(H)$. The paramagnetic contribution arises from the magnetic ions in intergranular boundaries or a non-superconducting impurity phase, e.g. Nd-422 [52], and is given by $M_P(H) = NgJ\mu_B B_J(gJ\mu_B H/(k_B T))$, where N is the number of the magnetic ions per unit volume, μ_B is the Bohr magneton, k_B is the Boltzmann constant, g is the Lande's g factor, J is the angular momentum quantum number, and B_J is the Brillouin function. However the presented experimental data demonstrate that an additional paramagnetic contribution appears at high temperatures and high magnetic fields. To describe the temperature evolution of the hysteretic curves, we extended the expression for the total magnetization:

$$M(H) = M_{S1}(H) + x_v(H; T)M_{P1}(H) + M_{P2}(H) \quad (13)$$

where lower indexes 1 and 2 are for superconducting and non-superconducting phases respectively, $M_{P1}(H)$ is the paramagnetic magnetization of unscreened magnetic ions occurred in the normal cores of the Abrikosov vortices, $x_v(H, T)$ is the fraction of the superconducting phase volume which occupied by vortex cores. The value of x_v increases with H and becomes equal to 1 at $H = H_{c2}$, where H_{c2} is the second critical field of the superconductor. The paramagnetic contribution of vortex cores was negligibly small at low T ($T < 60$ K) due to small x_v . Account of the vortex core

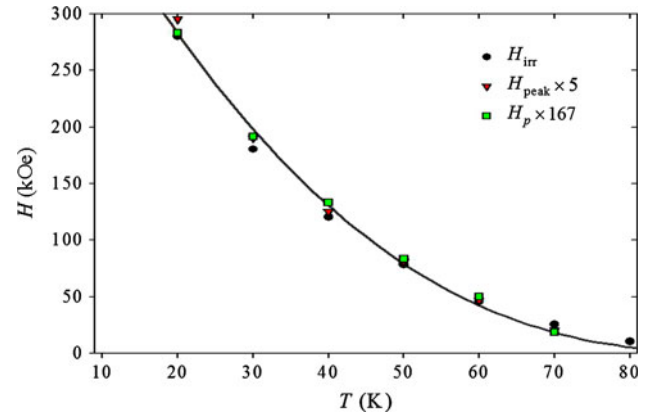


Fig. 9 Irreversibility field H_{irr} , peak field H_{peak} (increased in 5 times) and field of full penetration H_p (increased in 167 times) versus temperature. Solid line is $H(T) = 510 \text{ kOe} \times (1 - T/T_c)^{2.5}$

magnetization became important at high T ($T \geq 60$ K) as the vortex volume and x_v grow, $x_v(T) \sim \xi(T)^2$, here ξ is the superconductor coherence length.

The extended critical state model [53, 54] was applied to fit the $M_S(H)$ loops. The phenomenological formula for the local critical current density $j_c(B)$ was suggested to describe the hysteretic curve with the secondary peak:

$$j_c(B) = j'_c(B) \left(1 + A \exp \left(- \frac{\left(\frac{\ln |B|}{B_{\text{peak}}} \right)^2}{2 \left(\frac{B_w}{B_{\text{peak}}} \right)^2} \right) \right) \quad (14)$$

with a “unperturbed” decreasing field dependence of the critical current density

$$j'_c(B) = \frac{j_{c0}}{\frac{|B|}{B_0} + \exp \left(\frac{|B|}{B_1} \right)} \quad (15)$$

where j_{c0} is the critical current density at $B = 0$, B_0 and B_1 determine the decreasing rate in scales of low and high fields. The peak is described by its center position B_{peak} , the width B_w and the height A . Since an impurity phase was absent according to XRD analysis, the $M_{P1}(H)$ and $M_{P2}(H)$ functions were the same in the presented fitting. Given B_{peak} equal to experimental $\mu_0 H_{\text{peak}}$ values and Nd^{3+} ion parameters for $M_{P1}(H)$ and $M_{P2}(H)$, the hysteretic magnetization loops are successfully described for all temperatures. Solid lines on Fig. 6 are the fitting curves. The fitting parameters of the extended critical state model determine the full penetration field H_p . The values of H_{irr} , H_{peak} and H_p have similar temperature dependencies (Fig. 9) such that the scaling condition appears. Points on Fig. 9 are approximated by the power function $H(T) = 510 \text{ kOe} \times (1 - T/T_c)^{2.5}$.

Two scenarios are usually applied to explain the peak effect: a vortex lattice transition and a phase separation [55]. Scaling of $F_p(H)$ curves is evidence of the vortex

lattice transition [56, 57]. The plastic pinning scenario [58] predicts $H_{\text{peak}} \sim (1 - (T/T_c)^4)^{1.4}$ that does not agree with the $H_{\text{peak}}(T)$ dependence on Fig. 9. However the observed concave $H_{\text{peak}}(T)$ curve agrees with the line of the rhombohedral-to-square phase transition of the vortex lattice [59].

4 Conclusions

Nd(Ba,Nd)_{2.1}Cu₃O_{7- δ} system has been prepared by using solid-state reaction technique. The transport properties including structural/microstructural, electrical and magnetic properties of the system were investigated. We have found that the best heat treatment temperature/time combination is 1,020 °C for 24 h which is slightly lower than the peritectic temperature of the base YBCO-123 system. Microstructural properties were also improved at this temperature/time combination and the best T_c and T_0 values were obtained to be 93 and 89 K respectively.

Parameterization of hysteresis loops with the second peak was performed by the extended critical state model and the full penetration field was found. Correlated behavior of H_{irr} , H_{peak} and H_p and scaling of $F_p(H)$ curves sustain that the peak effect is caused by the vortex lattice transition.

The temperature dependence of thermoelectric power and thermal conductivity of the samples were also investigated in details. The TEP results were found to be positive for all the samples, suggesting that the dominant charge carriers are holes in all the samples.

Thermoelectric power analysis data were analyzed by “Modified Two Band Model with Linear T-Term” with modification for superconductors. The model was modified adding term, T^* , to normal band contribution. According to new equation (Eq. 5) and fitting parameters obtained a good agreement with experimental TEP data and fitting was obtained. For the thermal conductivity results of the samples prepared, a small peak with broad maximum was obtained just below T_c , which is attributed to the enhancement of the quasiparticle contribution to the thermal conductivity.

Acknowledgments The authors would like to thank Prof. M. E. Yakinci and Dr. S. Altin for their valuable discussions during to study.

References

1. L. Lei, G. Zhao, H. Xu, N. Wu, Y. Chen, Mater. Chem. Phys. **127**, 91 (2011)
2. S. Ye, H. Suo, Z. Wu, M. Liu, Y. Xu, L. Ma, M. Zhou, Physica C **471**, 265 (2011)
3. J. Jung, H. Darhmaoui, H. Yan, Supercond. Sci. Technol. **11**, 973 (1998)
4. M. Sparvieri, Mater. Chem. Phys. **28**, 133 (1991)
5. K. Salama, S. Sathyamurthy, Supercond. Sci. Technol. **11**, 954 (1998)
6. M.B. Turkoz, S. Nezir, A. Varilci, G. Yildirim, M. Akdogan, C. Terzioglu, J. Mater. Sci.: Mater. Electron. **24**, 1536 (2013)
7. M.B. Turkoz, S. Nezir, C. Terzioglu, A. Varilci, G. Yildirim, J. Mater. Sci.: Mater. Electron. **24**, 896 (2013)
8. K. Xu, K. Tsuzuki, S. Hara, D. Zhou, Y. Zhang, M. Murakami, D. Nishio-Hamane, M. Izumi, Supercond. Sci. Technol. **24**, 085001 (2011)
9. P. Pureur, J. Schaf, M.A. Gusmao, J.V. Kunzler, Physica C **176**, 357 (1991)
10. H.I. Adiguzel, M.A. Aksan, M.E. Yakinci, J. Mater. Process. Technol. **207**, 258 (2008)
11. S. Takekawa, H. Nozaki, Y. Ishizawa, N. Iyi, Jpn. J. Appl. Phys. **26**, L2076 (1987)
12. L. Dimesso, M. Marchetta, G. Calestani, A. Migliori, M. Masini, Supercond. Sci. Technol. **10**, 347 (1997)
13. W.M. Yang, L. Zhou, Y. Feng, P.X. Zhang, M.Z. Wu, Ch. Wende, X.Z. Wu, W. Gawalek, P. Gornert, Physica C **337**, 115 (2000)
14. K. Salama, A.S. Parikh, L. Woolf, Appl. Phys. Lett. **68**, 1993 (1996)
15. A.M. Hu, Z.X. Zhao, M.T. Su, T. Strasser, W. Gawalek, P. Gornert et al., Physica C **278**, 43 (1997)
16. S. Gong, D. Shi, G. Zhou, C. Cai, Y. Fu, H. Zhang, Proceeding of the International Workshop on Critical Current in Superconductors for Practical Application, World Scientific, (1997) 139
17. X. Yao, Y. Shiohara, Supercond. Sci. Technol. **10**, 249 (1997)
18. Z. Fan, W. Gao, F. Li, W. Jue, D. Soh, Physica C **386**, 241 (2003)
19. K. Takita, H. Kotoh, H. Akinaga, M. Nishino, T. Ishigaki, H. Asano, Jpn. J. Appl. Phys. **27**, L57 (1988)
20. P. Schätzle, G. Ebbing, W. Bieger, G. Krabbes, Physica C **330**, 19 (2000)
21. S. Neeleshwar, M. Muralidhar, M. Murakami, P.V. Reddy, Physica C **391**, 131 (2003)
22. J. Callaway, Phys. Rev. B **113**, 1046 (1959)
23. V. Florentiev, A. Inyushkin, A. Taldenko, O. Melnikov, A. Bykov, Proc. Internal. Conf. on transport properties of superconductors (ICTPS 90) (1990) 462
24. Y. Xu, J. Wurnig, M.J. Kramer, K.W. Dennis, R.W. McCallum, C.R. Schwichtenberg, A.R. Moodenbaugh, Physica C **294**, 194 (1998)
25. M. Sera, S. Shomoto, M. Sato, Solid State Commun. **68**, 649 (1988)
26. L. Forro, M. Raki, J.Y. Henry, C. Ayache, Solid State Commun. **69**, 1097 (1989)
27. V. Gottwick, K. Glass, F. Horn, F. Steglich, N. Greve, J. Magn. Mater. **47**, 536 (1985)
28. L. Forro, J. Lukatela, B. Keszei, Solid State Commun. **73**, 501 (1990)
29. R. Wang, H. Sekine, H. Jin, Supercond. Sci. Technol. **9**, 529 (1996)
30. B. Leon, A.D.S. Nag, J. Phys. F: Met. Phys. **5**, 1533 (1975)
31. T.R. Ravindran, V. Sankaranarayanan, R. Srinivasan, Pramana J. Phys. **39**, 109 (1992)
32. E. Natividad, M. Castro, R. Burriel, L.A. Angurel, J.C. Diez, R. Navarro, Supercond. Sci. Technol. **15**, 1022 (2002)
33. K. Knizek, M. Veverka, E. Hadova, J. Hejtmánek, D. Sedmidubsky, E. Pollert, Physica C **302**, 290 (1998)
34. R.C. Yu, M.B. Salamon, J.P. Lu, W.C. Lee, Phys. Rev. Lett. **69**, 1431 (1992)
35. M. Houssa, M. Ausloos, Physica C **257**, 321 (1996)
36. M.A. Aksan, M.E. Yakinci, J. Alloys Compd. **385**, 33 (2004)

37. M. Matsukawa, T. Mizukoshi, K. Noto, Y. Shiohara, *Phys. Rev. B* **53**, R6034 (1996)
38. M. Ausloss, M. Houssa, *Supercond. Sci. Technol.* **12**, R103 (1999)
39. F. Yu, M.B. Salaman, V. Kopylov, N.N. Kolesnikov, H.M. Duan, A.M. Hermann, *Physica C* **235–240**, 1489 (1994)
40. T. Plackowski, A. Jezowski, Z. Bukowski, *Z. Phys. B* **104**, 745 (1997)
41. M. Matsukawa, T. Mizukoshi, K. Noto, Y. Shiohara, *Phys. Rev. B* **53**, R6034 (1996)
42. R.M. Bhatt, R.P. Gairola, *Curr. Sci.* **80**, 864 (2001)
43. F. Bazdidi-Tehrani, M.H. Kamrava, *World Acad. Sci. Eng. Technol.* **80**, 167 (2011)
44. J. Bardeen, G. Rickayzen, L. Tewordt, *Phys. Rev.* **113**, 982 (1959)
45. E.D. Ramos, D.H. Sanchez *Cryogenics* (1974) 341
46. J. Bardeen, G. Rickayzen, L. Tewordt, *Phys. Rev.* **113**, 982 (1959)
47. C.K. Subramaniam, H.J. Trodahl, A.B. Kaiser, B.J. Ruck, *Phys. Rev. B* **51**, 3116 (1995)
48. C.P. Bean, *Phys. Rev. Lett.* **8**, 250 (1962)
49. D. Dew-Hughes, *Phil. Mag.* **30**, 293 (1974)
50. E.J. Kramer, *J. Appl. Phys.* **44**, 1360 (1973)
51. V. Sandu, *Mod. Phys. Lett. B* **26**, 1230007 (2012)
52. N. Hari Babu, T. Rajasekharan, L. Menon, S. Srinivas, S.K. Malik, *Physica C* **305**, 103 (1998)
53. D.M. Gokhfeld, D.A. Balaev, M.I. Petrov, S.I. Popkov, K.A. Shaykhtudinov, V.V. Valkov, *J. Appl. Phys.* **109**, 033904 (2011)
54. D.M. Gokhfeld, *J. Supercond. Nov. Magn.* **26**, 281 (2013)
55. M. Nakamura, Y. Yamada, T. Hirayama, Y. Ikuhara, Y. Shiohara, S. Tanaka, *Physica C* **259**, 295 (1996)
56. D. Dew-Hughes, *Phil. Mag.* **30**, 293 (1974)
57. M.R. Koblishka, A.J.J. van Dalen, T. Higuchi, S.I. Yoo, M. Murakami, *Phys. Rev. B* **58**, 2863 (1998)
58. Y. Abulafia, A. Shaulov, Y. Wolfus, R. Prozorov, L. Burlachkov, Y. Yeshurun, D. Majer, E. Zeldov, H. Wuhl, V.B. Geshkenbein, V.M. Vinokur, *Phys. Rev. Lett.* **77**, 1596 (1996)
59. B. Rosenstein, B.Y. Shapiro, I. Shapiro, Y. Bruckental, A. Shaulov, Y. Yeshurun, *Phys. Rev. B* **72**, 144512 (2005)